applied optics

Polarized-depolarized Rayleigh scattering for simultaneous composition and temperature measurements in non-isothermal gaseous mixtures

KHARTHIK CHAKRAVARTHY,* LAURENT M. LE PAGE, AND BENJAMIN A. O. WILLIAMS

Department of Engineering Science, University of Oxford, Oxford OX2 0ES, UK
**kharthikchakravarthy@gmail.com*

Received 9 September 2022; revised 4 February 2023; accepted 1 March 2023; posted 1 March 2023; published 11 April 2023

This paper demonstrates the application of polarized-depolarized Rayleigh scattering (PDRS) as a simultaneous mixture fraction and temperature diagnostic for non-reacting gaseous mixtures. Previous implementations of this technique have been beneficial when used for combustion and reacting flow applications. This work sought to extend its applicability to non-isothermal mixing of different gases. The use of PDRS shows promise in a range of applications outside combustion, such as in aerodynamic cooling technologies and turbulent heat transfer studies. The general procedure and requirements for applying this diagnostic are elaborated using a proof-of-concept experiment involving gas jet mixing. A numerical sensitivity analysis is then presented, providing insight into the applicability of this technique using different gas combinations and the likely measurement uncertainty. This work demonstrates that appreciable signal-to-noise ratios can be obtained from this diagnostic in gaseous mixtures, yielding simultaneous temperature and mixture fraction visualization, even for an optically non-optimal selection of mixing species.

https://doi.org/10.1364/AO.472996

1. INTRODUCTION

Simultaneous determination of gaseous mixture fraction and temperature is an important capability in fluid dynamic research. Some applications that would benefit from this include high-speed aerothermodynamics (such as in quantifying the effectiveness of active thermal protection systems [1,2]), gas turbine blade cooling technologies (such as effusion and film cooling [3,4]), exhaust gas recirculation systems [5], and fundamental turbulent heat transfer studies [6]. In order to accurately determine mixture fraction and gas temperature, there are a variety of techniques available depending on the parameter and location of interest. For example, physical sensors can be used to sample the flow at discrete locations along a specified path. However, in the case of gas composition, some sensor types are known for their low species selectivity and inconsistent signal response, resulting in both poor spatial resolution and low accuracy [7–9]. Thermocouples are the obvious choice when seeking to measure temperature at a given position. However, their use in high-temperature environments requires corrections for radiative and conductive losses and can be complicated by uncertainties in convective heat transfer coefficient, geometry, and emissivities [10,11]. In general, the use of discrete physical sensors limits spatial resolution, while intruding and influencing the flow of interest, providing limited and inaccurate information. Pressure- and temperature-sensitive paints (PSPs and TSPs) can provide minimally intrusive spatially resolved measurements by their application to a surface [12], but these lack resolution in the wall-normal direction, that is, within the fluid.

To spatially resolve the mixing of gases away from a surface, advanced laser diagnostics are more applicable. Two-dimensional flow visualization using laser diagnostics has been well established in the fields of fluid mechanics and combustion. These techniques use illumination of the flow of interest with a laser sheet, producing a signal that is typically recorded orthogonally using a sensitive camera or other photodetector. Rayleigh scattering is one such technique that has widely been used to yield species composition, temperature, density, velocity, and pressure measurements [13,14]. Rayleigh scattering arises from the incoherent scattering of light from particles that are significantly smaller than the wavelength of the incident illumination. If interrogating a singular gas species, this technique can be used to map a temperature field with dimensions only limited by the light sheet geometry [15]. For an isothermal non-reacting gas

mixture, it is possible to map the mixture fraction of each gas from the Rayleigh signal [16–19].

There is a limitation for Rayleigh scattering in that it is not trivial to independently or simultaneously measure mixture fraction and temperature for a non-isothermal combination of gases. To date, this limitation has been addressed by combining Rayleigh scattering with a separate simultaneous diagnostic. Several works from Stårner *et al.* [20–23] employed simultaneous Raman scattering to obtain mixture fraction measurements that would enable temperature evaluation from Rayleigh signals. Sevault *et al.* [24] performed an identical technique in his investigations of oxy-fuel flames. Frank *et al.* [25] demonstrated the use of acetone and acetaldehyde laser-induced fluorescence (LIF) in tandem with Rayleigh measurements for extraction of composition information. Each of these has associated disadvantages or limitations to their use. For example, LIF measurements require the use of specific wavelength excitation sources and flow tracers. LIF measurements are also temperature-dependent, making isolation of composition effects non-trivial. Raman scattering generally yields weak signals (about 3 orders of magnitude weaker than Rayleigh scattering), giving low signal-to-noise (SNR) measurements.

Alternatively, polarized-depolarized Rayleigh scattering (PDRS) has been used to obtain simultaneous spatially resolved temperature and mixture fraction measurements of combustion and flames [26–29]. PDRS extends traditional Rayleigh scattering measurements by exploiting the polarization state of the scattered light, yielding a more quantitative measurement. PDRS, as with Rayleigh scattering, uses a linearly polarized laser sheet, where the majority of light scattered from gas molecules remains in the same polarization state as the incident light. This light is termed "polarized" light. Advantageously, many molecules scatter a smaller fraction of light (less than 7%) in the orthogonal polarization state, due to the molecules' lack of spherical symmetry. This weaker component, termed "depolarized" light, provides an order of magnitude improvement in signal strength as compared to Raman scattering, making it a promising option.

In the works of Fielding *et al.* [26], no attempt to reconstruct the mixture fraction or temperature from PDRS was conducted. Instead, modeled and measured signals were presented. The works of Frank *et al.* [27,28] extracted 2D mixture fraction and temperature fields from PDRS; however, they used a so-called three scalar approach, which required the use of CO-LIF in tandem. In addition, a complete and thorough implementation and processing procedure is lacking in these previous works. This paper seeks to fill this gap by providing a detailed PDRS procedure and analysis to make the method more accessible for applications other than combustion.

Although PDRS has been used several times in reacting flows, the technique has the potential to also be employed in non-reacting flow applications to spatially resolve both gas composition and temperature. A specific application that would benefit from PDRS is effusion cooling of turbine blades. PDRS would enable coolant and free-stream gases to be distinguished, allowing quantification of cooling effectiveness (a measure of how well coolant spreads) and temperature. This information could be used in informing design approaches and CFD models when developing next-generation cooling technologies. A key difference between such an application and combustion is the need to use gases that are more relevant to wind-tunnel applications, such as air or N_2. To this end, the work presented in this paper will detail the application of PDRS to a simple binary gas mixture to investigate its applicability and limits. Specifically, a dual-jet flow of CO_2 adjacent to a heated flow of N_2 will be interrogated to generate 2D mixture fraction and temperature maps. Additionally, this paper will outline the measurement sensitivity and uncertainty of PDRS when analysing other gas combinations.

2. POLARIZED-DEPOLARIZED RAYLEIGH SCATTERING

A. Theory

In "standard" Rayleigh scattering, incident light induces a dipole in gas molecules and is re-radiated without loss of energy (elastic scattering). The light intensity produced by Rayleigh scattering, I_R, is proportional to the incident light intensity, I_o, the effective Rayleigh scattering cross-sectional area of the gas, σ_R, and bulk density, ρ, as described by Eq. (1),

$$I_R \propto I_o \rho \sigma_R. \tag{1}$$

For ideal gases, ρ at any point in a gas can be expressed in terms of the local pressure and temperature, according to Eq. (2),

$$\rho = \frac{p}{RT}, \tag{2}$$

where p is the pressure of the gas, R is the specific gas constant, and T is the temperature of the gas. Substituting Eq. (2) into Eq. (1) expresses the Rayleigh signal as inversely proportional to temperature at a point within a gas

$$I_R \propto I_o \frac{\sigma_R}{T}. \tag{3}$$

Given this, Rayleigh scattering has extensively been used as a diagnostic technique to measure the temperature of a gas. The inherent assumption here is that the pressure of the gas is spatially uniform and constant with time, which is typically valid for many applications, notably flames.

A significant challenge when using Rayleigh signals for thermometry in multi-component flows is evaluating σ_R,

$$\sigma_R = \sum_i z_i \sigma_{R,i}, \tag{4}$$

where z_i and $\sigma_{R,i}$ are the mixture fraction and the Rayleigh cross-sectional area of gas i, respectively. The mixture fraction quantifies the extent of mixing between gases, taking on a value between 0 (no gas i present) and 1 (only gas i present). In applications in which a mixture of gases is involved, it becomes difficult to estimate z_i at every domain location. This becomes harder when species react with each other to form new species, such as in combustion. Experimentalists have tried to estimate σ_R through a number of methods. Smith [30] obtained σ_R by simulating their combustion process in order to obtain species composition as a function of space. Another approach taken by Bergmann *et al.* [31] and Dibble and Hollenbach [32] involved

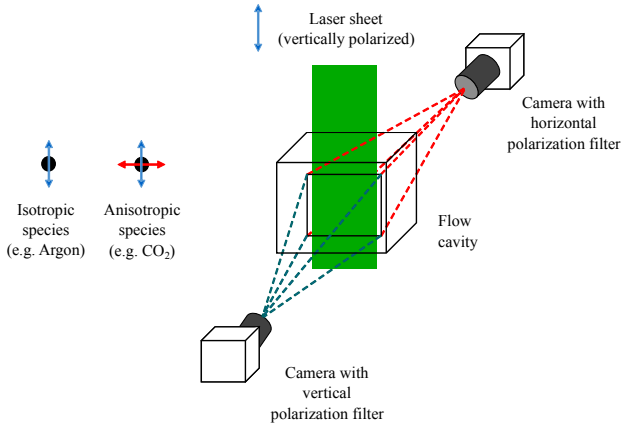

Fig. 1. Illustration of a typical PDRS setup. Blue lines correspond to vertically polarized light, while red lines correspond to horizontally polarized light.

choosing fuel–oxidizer combinations that would result in a relatively constant σ_R. The need to control or numerically estimate σ_R limits the applicability of Rayleigh scattering for thermometry of gaseous mixtures.

PDRS can tackle the problem of accurately determining σ_R, depending on the gases used. The fraction of "depolarized" light scattered in the orthogonal polarization state to that of the incoming laser light is called the depolarization ratio, r_p, defined according to Eq. (5),

$$r_p = \frac{I_{dep}}{I_{pol}}, \tag{5}$$

where I_{dep} is the intensity of orthogonally polarized scattered light ("depolarized") and I_{pol} is the intensity of scattered light in the same polarization state as the laser ("polarized"). Note that r_p varies depending on the wavelength of the laser used. Values of r_p used in this paper have been taken from [26,33]—only those at 532 nm laser illumination have been quoted. In a binary gaseous mixture, regions containing pure gas 1 and pure gas 2 would have r_p values equal to that of gas 1 and gas 2, respectively. Regions where gases have mixed will have an intermediate r_p value, which is dictated by the mixture fraction, z_i, of each gas. This distribution of r_p for different values of z_i can be numerically modeled, knowing individual r_p values of the chosen gases at the laser wavelength.

In PDRS, two cameras are used to capture Rayleigh signals; each camera is fitted with polarization filters oriented in orthogonal directions to one another, as shown in Fig. 1. By taking the ratio of pixel intensities from both cameras at the same spatial locations, a value for r_p at that point can be obtained. The mixture fraction of each gas may then be evaluated by linear interpolation of the modeled relationship between r_p and z_i. Subsequently, σ_R can be calculated at every point in the domain, enabling temperature measurement using the normal Rayleigh method [Eq. (1)].

Previous implementations of PDRS have applied what is typically referred to as "difference Rayleigh scattering" in flame investigations [26–29]. These have involved linear or non-linear combinations of I_{pol} and I_{dep} to provide a metric (known as the difference Rayleigh signal) for fuel concentration. In modeling the variation of the difference Rayleigh signal as a function of mixture fraction, temperature dependence is not isolated; that is, chemical models must be used to model the species concentration and temperature at every mixture fraction. Here, an inherent assumption is made that the chemical models accurately account for species concentration and temperature variations as a function of mixture fraction. Alternatively, a three-scalar approach was used to uncouple the effect of temperature, as performed by Frank *et al.* [27,28]. In the current work, a direct evaluation of r_p is made since I_{dep} is divided directly by I_{pol}. The dependence on all other quantities such as laser energy, temperature, and pressure cancel out. This method is beneficial since it makes no prior assumptions of the system behavior, and it does not rely on an additional diagnostic. This paper represents the first-ever demonstration of such a processing methodology.

Table 1. List of r_p and Relative σ_R Values for Some Candidate Gases in PDRS at 532 nm[a]

Gas	r_p (%)	$\sigma_R/\sigma_{R,N_2}$
Ar	0	0.87
He	0	0.01
H_2	0.90	0.21
N_2	1.06	1
O_2	2.94	0.86
CO_2	4.08	2.39
CO	0.51	1.24
CH_2	0.02	2.13

[a]Data presented here were collected from works by Sutton and Driscoll [34], Fuest *et al.* [33], and Gardiner *et al.* [35].

B. Challenges

1. Choice of Gases

PDRS requires the chosen gases to have different r_p values to enable linear interpolation of z_i. The larger the disparity in r_p, the more sensitive the technique becomes. Table 1 lists r_p and relative σ_R values for several candidate gases for PDRS (note that values quoted here are for 532 nm illumination).

Noble gases like argon and helium are valued in PDRS experiments as they have zero depolarization. These are then paired with highly anisotropic molecules like CO_2 to produce large disparities in r_p, thus maximizing the technique's sensitivity.

2. Signal-to-Noise Ratio

High laser pulse energies are typically required for Rayleigh scattering since gases have small scattering cross sections. The desire to measure the depolarized component requires even larger pulse energies since depolarized signals are about 2 orders of magnitude weaker than their polarized counterparts. Notably, Frank *et al.* [27,28] used 1.8 J of pulse energy for appreciable SNR. Signal amplifying cameras, such as intensified or electron-multiplying charge-coupled devices (CCDs), are typically required for this technique, especially for the depolarized signal component. Some previous investigations have succeeded in attaining sufficient polarized Rayleigh signal using non-intensified CCD cameras, as shown in works from Frank *et al.* [27,28].

3. APPLICATION TO NON-ISOTHERMAL GASEOUS MIXTURES

In this proof-of-concept experiment, simultaneous composition and temperature measurements were extracted from a dual-jet mixed flow—a plan view schematic of the experimental layout is shown in Fig. 2. A cold CO_2 jet was produced adjacent to a hot N_2 jet in static atmosphere. Both these jets were enclosed in a co-flow of cold N_2—this was to prevent entrainment of dust particles into the experimental field of view. Mass flow controllers (Omega FMA-2609A and Omega FMA5520A) regulated the flow rate of each jet to 8 slpm. The hot flow was created by passing cold N_2 through an inline resistive heater (Omega AHP-5052). The voltage supplied to the heater was varied using an autotransformer in order to adjust the heat input to the gas.

The flow was probed with a 650 mJ vertically polarized laser pulse from a Continuum Powerlite Nd:YAG laser operating at its second-harmonic wavelength of 532 nm. A Thorlabs Glan–Taylor calcite polarizer with an extinction ratio of 10^5:1 was used to remove other polarization components. This beam was formed into a 6 mm vertical sheet using a $f = 500$ mm cylindrical lens. Scattered "polarized" and "depolarized" light from the interaction region was acquired using two opposite-facing Princeton Instruments intensified charge-coupled device cameras (ICCD-512T and ICCD-576GRB), each fitted with 85 mm $f/1.2$ Mitakon Speedmaster lenses and orthogonally oriented polarization filters (B + W XS-Pro Digital Käsemann). The laser sheet came to a focus at the center of the jets and the cameras' field of view.

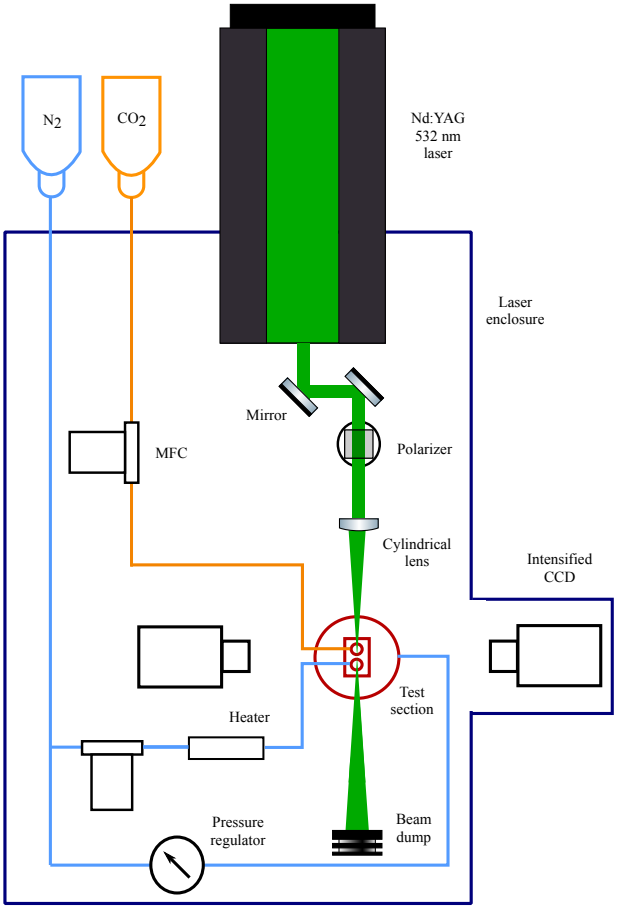

Fig. 2. Plan view schematic of PDRS proof-of-concept experimental layout.

The polarization filters' angular positions were calibrated to minimize leakage of polarized and depolarized light into the unintended camera. This was achieved by collecting signals from just the N_2 co-flow (with both jets turned off) for a range of filter angular positions. The average signal from 50 images was evaluated at each filter position and subsequently plotted. Maxima indicated positions where the filter was aligned with the Rayleigh signal's main polarization component (i.e. the "polarized" component), while minima indicated the opposite. Thus, in the experiment, the camera used to image the "polarized" Rayleigh component was set to the filter angular position that maximizes signal, while that of the "depolarized" Rayleigh component was set to the filter angular position that minimizes signal.

Prior to conducting the experiment, the r_p values of N_2 and CO_2 were verified, in order to ensure that the subsequent data post-processing would yield reliable results. Gain settings on each ICCD were adjusted to produce appreciable signals for depolarized N_2 (being the weakest)—these settings were maintained for the proof-of-concept experiment. Images were then collected using a single camera at both polarized and depolarized filter orientations (independently) for both gases in isolation. A ratio was then determined using average polarized and depolarized signals. The r_p values obtained were found to tally with literature values given in Table 1. This procedure was conducted on both cameras as an added check for ICCD non-linearity, as deviation from published r_p values could imply that the cameras were operating in a non-linear regime. It is important to note that the PDRS processing method could be compromised if the ICCDs operate outside the linear regime, so such a verification procedure should be performed to confirm the maximum usable ICCD gain. Note that this could limit the achievable SNR. Replacing the ICCDs with electron-multiplying CCD cameras may provide better linearity.

Mixture fraction evaluation during post-processing of results required pixel-by-pixel division of the polarized and depolarized images, each coming from separate cameras. In order to ensure accurate spatial mapping of pixels across both cameras, a double-sided grid pattern was placed in the field of view and imaged. Pixel coordinates of grid corners from both cameras were extracted using the open source MATLAB Camera Calibration Toolbox produced by California Institute of Technology [36]. These were used as control points to evaluate a transformation that would accurately map depolarized signals onto polarized signals. Subsequently, this transformation was applied to all acquired depolarized signals to achieve spatial mapping.

After filter calibration and grid imaging, tests were initiated by turning on mass flow controllers to the desired flow rate. N_2 jet heating commenced by increasing the voltage set on the autotransformer. A thermocouple was placed above the hot jet—temperatures were logged using a PicoScope TC-08 thermocouple logger and monitored until steady-state conditions were achieved. Finally, the thermocouple was removed (to avoid overwhelming Mie scatter), and the laser aperture was opened, sending pulses toward the imaging area. Images were

simultaneously acquired on both cameras using a gate of 500 ns at a frequency of 1 Hz.

A number of post-processing steps were applied to the images in order to extract mixture fraction and temperature. A summary of this procedure is presented in Fig. 3. After image registration, shot-to-shot background signals were evaluated by averaging pixel values in image regions outside laser illumination. These background values were subtracted from all polarized and depolarized images, as shown in Figs. 3(a) and 3(b). Laser energy fluctuations and non-uniform sheet intensity profiles were corrected by dividing each polarized and depolarized image with a sheet correction map, shown in Figs. 3(c) and 3(d). This was obtained by separately averaging the left and right 10 pixel columns (where co-flow was present) from each polarized image to produce two vertical sheet profiles and subsequently interpolating these profiles across the entire image. Note that using the depolarized signal to correct for sheet intensity fluctuations would lead to noisy results since the depolarized signal in the co-flow was small in comparison. Next, strong scatter from stray particles was filtered from images by masking saturated pixels using image thresholding and inward interpolation of pixel values surrounding specified masked regions, demonstrated in Figs. 3(e) and 3(f). Finally, depolarized signals, shown in Fig. 3(g), were divided by polarized signals to produce r_p maps, shown in Fig. 3(h).

Since two separate cameras were used, each using different gain settings and image configurations, r_p maps obtained were proportional to actual r_p of the gases used. The average value in the pure N_2 region was used to normalize and convert these maps into values corresponding to the actual gas r_p. Next, a lookup curve was generated, from which r_p values were converted into a mixture fraction map, as shown in Fig. 3 (i). Pixels exhibiting values larger than 1 or smaller than 0 due to noise were set to their respective limiting values. Final composition maps were then used to calculate the effective scattering cross section at each pixel. This was then divided by the sheet-corrected polarized signals in order to produce a map that is proportional to temperature. Lastly, these maps were scaled to realistic temperatures using steady-state values measured on the thermocouple. This produced temperature maps as shown in Fig. 3(j).

Figure 4 shows the obtained results after post-processing. Here, each row represents a pair of single-shot composition and temperature maps. As before, mixture fraction values of 1 indicate pure CO_2 while values of 0 indicate pure N_2. A pixel size of 28 μm was achieved.

Mixture fraction maps show two distinct regions, i.e., regions occupied mostly by CO_2 as well as regions occupied by pure N_2. Radial composition gradients are evident in the CO_2 jet region, indicating entrainment of surrounding N_2 from the co-flow, as well as the hot jet. Temperature maps on the other hand indicate three distinct regions. The high temperatures of the hot N_2 are immediately noticeable—steady-state temperatures of 415 K were achieved at the base of the hot N_2 jet. Vertical temperature gradients are also evident, indicating a gradual loss of heat from the jet to the surroundings as it convects upward. The temperature in the co-flow is moderate and exhibits close agreement with room temperature—a mean temperature of 297 K was obtained across 250 images. CO_2 jet regions display the lowest

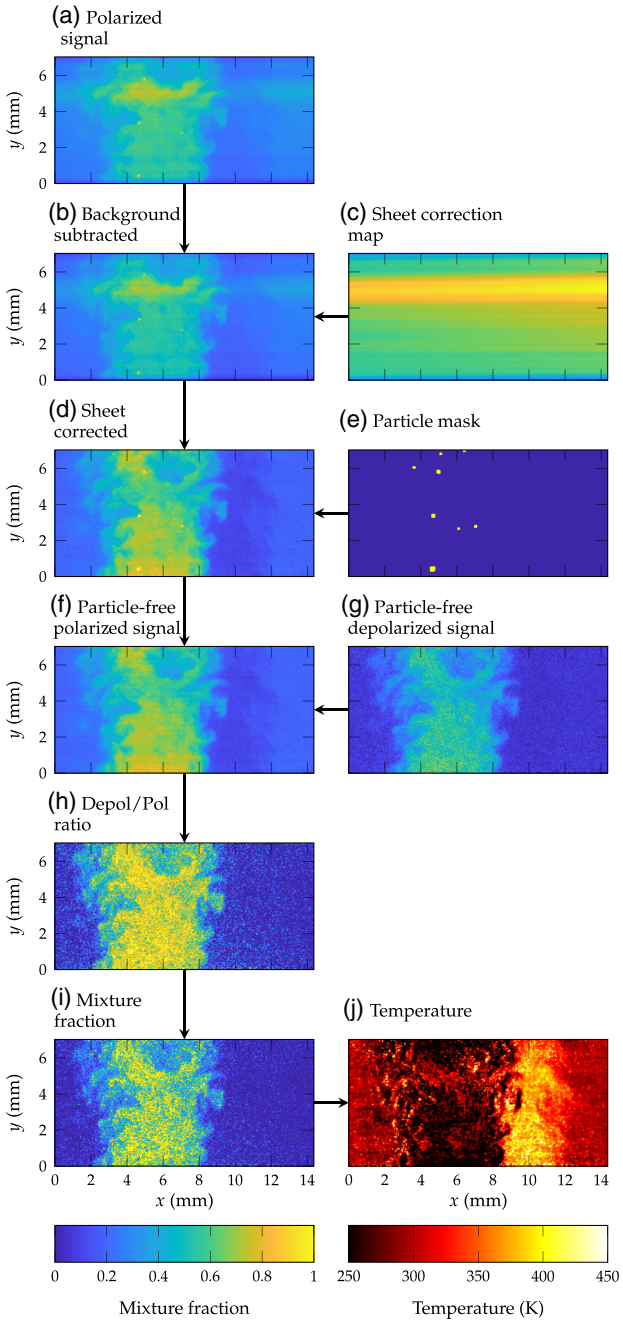

Fig. 3. Post-processing procedure of extracting mixture fraction and temperature from PDRS. Color bars for intermediate steps have been omitted for simplicity.

temperatures, with a mean value of approximately 271 K across 250 images as a result of gaseous CO_2 being supplied to the nozzle after a phase change.

To demonstrate the virtue of such measurements, Fig. 5 shows the first three composition modes of the dual-flow configuration obtained by applying proper orthogonal decomposition (POD) to the data collected. POD decomposes data from a fluctuating time series into a sequence of orthogonal modes, ordered from highest to lowest energies. It is typically used in the field of fluid mechanics as an indicator of coherent structures in a flow. For brevity, POD modes for mixture

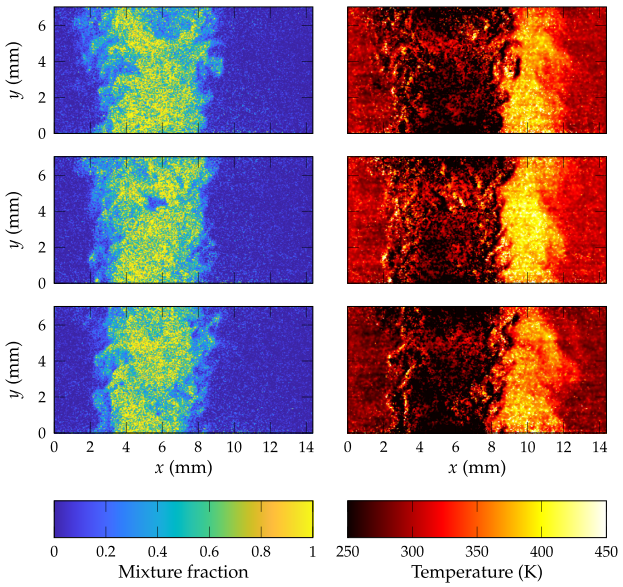

Fig. 4. Single-shot mixture fraction and temperature pairs from dual-flow experiment. A mixture fraction of 1 refers to CO_2, while a mixture fraction of 0 refers to N_2.

fraction fields are presented here, but the analysis may also be applied to temperature fields. Modes were evaluated by subtracting the mean mixture fraction field from individual snapshots and subsequently evaluating the singular value decomposition of the mixture fraction time series (250 images).

The POD modes highlight regions exhibiting relevant strong mixing structures. Here, a range of large and small scale structures are visible, particularly in the central CO_2 jet region (as seen in Mode 1), along the right hand shear layer between CO_2 and N_2 jets (as seen in Mode 2) and along the left hand shear layer between the CO_2 jet and N_2 co-flow (as seen in Mode 3). Mode 1 indicates large scale mixing taking place at the upper region of the field of view, that is, as the CO_2 jet convects upward and expands laterally. Mode 2 highlights smaller sized alternating mixing structures that form between the jets that have similar upward convection speeds. Mode 3 shows that mixing between the CO_2 jet and the co-flow forms larger sized alternating structures, perhaps as a result of the discrepancy in upward convection speeds.

Results from this proof-of-concept experiment have demonstrated that simultaneous quantitative measurements are achievable for a binary non-isothermal gas mixture. Single shot 2D temperature and mixture fraction fields are obtainable as shown in Fig. 4, in which the effect of gas mixing can be seen clearly. The minimum SNR (defined as the signal divided by background noise) in this configuration was 1.85 ± 0.08, obtained in the depolarized signal from the hot N_2 jet. The maximum SNR was 13.15 ± 3.64, corresponding to the polarized signal from the CO_2 jet. These values are modest when compared to SNRs achieved in other applications of PDRS [27,28]. The effect of noise is evident from the lack of uniformity in supposed uniform regions of reconstructed images, for example, bright spots in the mixture fraction maps in areas only containing N_2. Smoothing of images using Gaussian, or other, filters would remove these artifacts at the expense of reduced

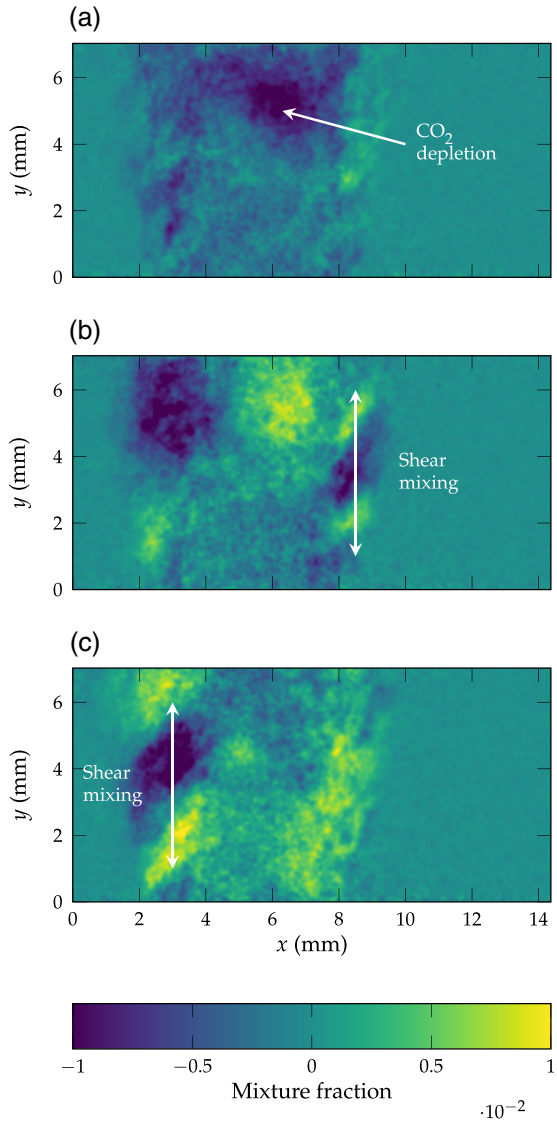

Fig. 5. First three mixture fraction POD modes of the dual-jet flow configuration. (a) Mode 1, (b) Mode 2, and (c) Mode 3.

spatial resolution. Future studies involving PDRS would benefit from taking steps toward improving the SNR, such as using higher pulse energies or more sensitive cameras, so that reconstructed temperature and composition fields are more clean and exhibit minimal noise.

4. SENSITIVITY ANALYSIS

In order to inform future PDRS experiments, a numerical investigation of the sensitivity of this technique was performed. PDRS is most effective when the gaseous species used differ substantially in r_p, as described in Section 2.B. When performing PDRS, the depolarized signal captured by one camera is divided by the polarized signal captured by another camera to produce a 2D distribution of r_p. If two gases are used, this distribution will have r_p values between those of the two gases. By using two gases that differ substantially in r_p, the measured distribution will exhibit high contrast, making interpolation of the gas mixture fraction more accurate.

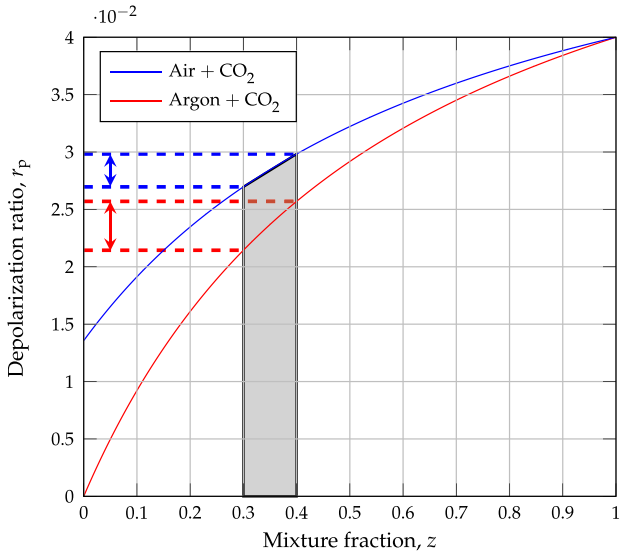

Fig. 6. Graph showing sensitivity to changes in mixture fraction when using air/CO_2 (blue line) and argon/CO_2 (red line). Note how it takes a smaller range of r_p values to produce the same mixture fraction uncertainty (gray area) when using air/CO_2 (blue double-sided arrow) as compared to argon/CO_2 (red double-sided arrow).

As the r_p values of each gas get closer to one another, PDRS becomes susceptible to noise; small fluctuations in measured r_p lead to large changes in predicted mixture fraction. Figure 6 shows a typical lookup curve generated from simulating polarized and depolarized Rayleigh signal intensities. It is evident that the measurement sensitivities differ for different gas combinations. Argon has a r_p value of 0, while CO_2 has a r_p value of 4.08% [33]. The combination of CO_2 and argon produces a large disparity in r_p values. On the contrary, air has a r_p value of ~1.40%, meaning CO_2 and air mixtures span a smaller range of r_p values. Shallow gradients imply higher uncertainty, as small changes in r_p lead to large changes in mixture fraction. This becomes a problem when the SNR of a Rayleigh image is low. To this end, the following analysis attempts to quantify and compare the expected uncertainty when using PDRS with different gas combinations. Two mixtures are investigated here: argon with CO_2 (representing the ideal case which maximizes r_p disparity) and air with CO_2 (representing a more economical gas mixture).

To assess the level of uncertainty for different gas combinations, the Poisson noise characteristic from a camera was used to model "best-case" fluctuation in Rayleigh signals. Figure 7(a) shows a histogram of pixel counts obtained from a CCD camera (ImperX 1M48-G) imaging a white target. The pixel intensities are distributed according to a Poisson distribution due to fluctuations in the number of photons reaching the CCD sensor. At higher average intensities, this fluctuation can be approximated by a normal distribution, as shown in Fig. 7(a). Poisson noise becomes less apparent in brighter images as it contributes a smaller fraction of the total measured signal, and it becomes more apparent in darker images as it can contribute a larger fraction of the total measured signal [37]. This poses a problem for depolarized Rayleigh signals, as they are 2 orders of magnitude less bright than their polarized counterparts. In this investigation, Poisson noise estimates from this CCD camera

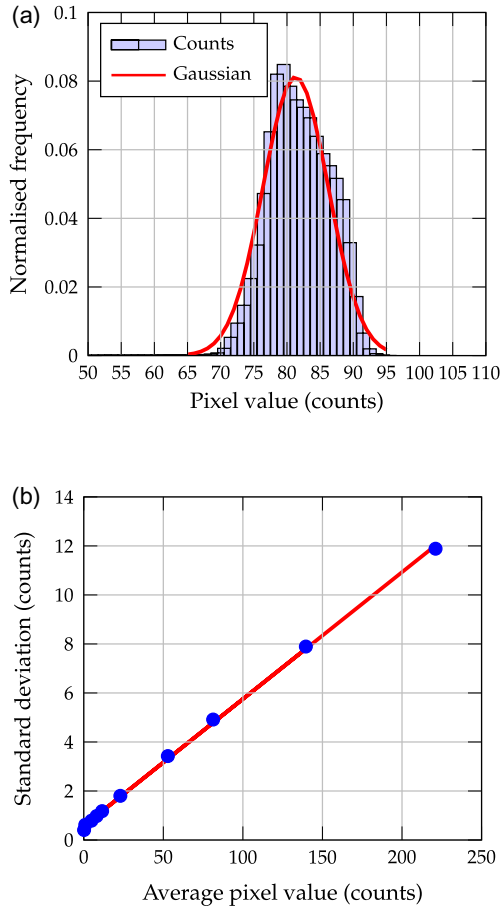

Fig. 7. (a) Example histogram of CCD pixel counts, fitted with a normal distribution and (b) a graph showing the relationship between average number of counts and standard deviation of the fitted distribution.

were used to quantify PDRS measurement uncertainties for different gas combinations. By imaging a white target with varying aperture size, Gaussian profiles were fitted to signal histograms acquired at varying sensor illumination levels. A graph of standard deviation against mean pixel intensity was then plotted, shown in Fig. 7(b); the gradient of this graph was used to scale the simulated measurement error, in the subsequent uncertainty analysis.

To investigate the uncertainty in PDRS measurements, a simulated mixture fraction and temperature map was modeled. Figure 8 shows the arbitrary simulated maps used in this investigation. Polarized and depolarized Rayleigh signals were constructed by substituting these maps along with the Rayleigh scattering cross-sectional area σ_R and r_p for each gas into Eq. (1) and Eq. (5) (refer to Table 1 for σ_R and r_p values used).

Subsequently, a Gaussian noise fluctuation was introduced to both the polarized and depolarized signals at every pixel; the amplitude of this fluctuation was obtained by multiplying the pixel intensity by the gradient obtained in Fig. 7(b). Finally, these simulated Rayleigh signals were processed using the previously elaborated PDRS procedure to recreate the input mixture fraction and temperature map. Figure 9 shows the reconstructed fields; the effect of the noise is immediately apparent when comparing these images with the input maps.

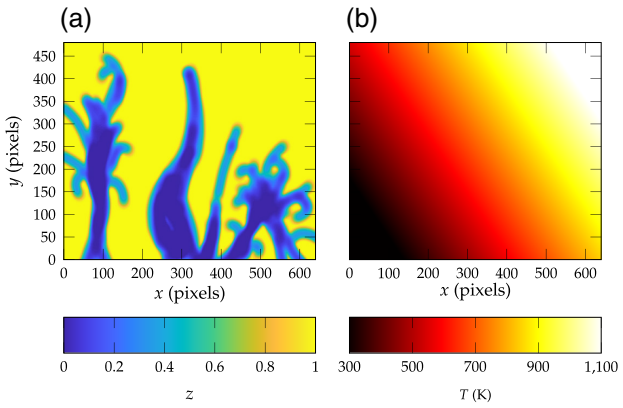

Fig. 8. Simulated (a) mixture fraction and (b) temperature fields. A mixture fraction of 1 refers to CO_2, while a mixture fraction of 0 refers to air/argon.

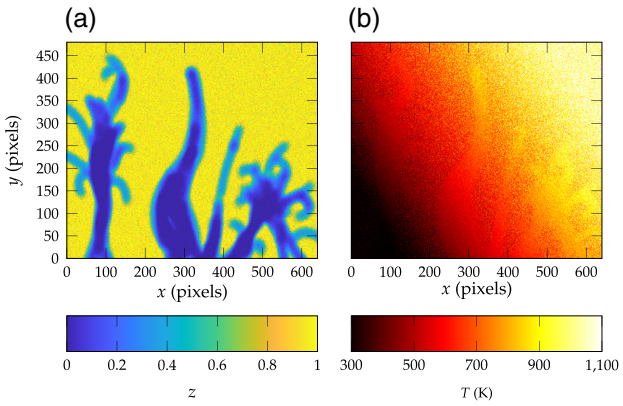

Fig. 9. PDRS-reconstructed mixture (a) fraction and (b) temperature fields with added noise. A mixture fraction of 1 refers to CO_2, while a mixture fraction of 0 refers to air/argon.

By subtracting the input fields from the reconstructed fields, an uncertainty distribution was obtained, as shown in Fig. 10 for mixture fraction. There are two distinct regions of uncertainty in this map, a result of the different r_p in each area. High error regions correspond to CO_2, which has a high r_p, while low error regions correspond to air or argon, which have lower r_p. While this may seem counterintuitive, the reason for this behavior is a dampening of noise fluctuations in the depolarized signal when dividing by the much larger polarized signal to obtain r_p. In order to quantify an effective uncertainty for this reconstruction, two approaches were taken. In the first approach, the maximum uncertainty from the noise map was defined as the global uncertainty. The second approach involved segmenting regions of low and high error, and averaging them independently—this is shown in Fig. 11. A global mean uncertainty was then defined as the average of both the low and high mean uncertainties.

To simulate taking multiple Rayleigh pictures and averaging the results, the aforementioned analysis was repeated for multiple images per sequence. Figures 12 and 13 show the relative uncertainty distributions for both uncertainty approaches. The horizontal axis in both figures is drawn on a logarithmic scale.

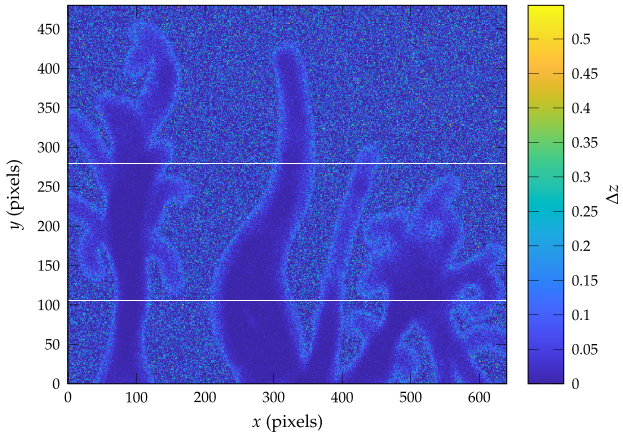

Fig. 10. Uncertainty map in reconstructed mixture fraction image. Horizontal profiles extracted from rows 105 and 280, indicated as white lines, are shown in Fig. 11.

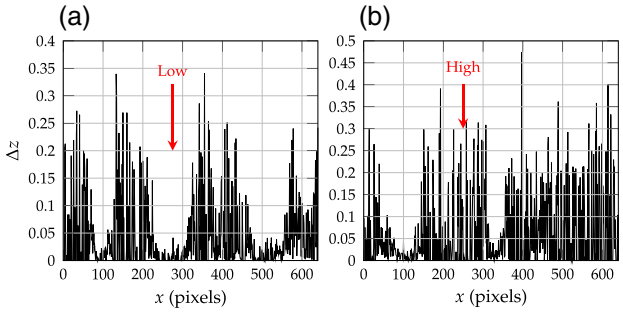

Fig. 11. Error data extracted from rows (a) 105 and (b) 280. The data possess regions of high and low amplitude fluctuations as illustrated by the annotations.

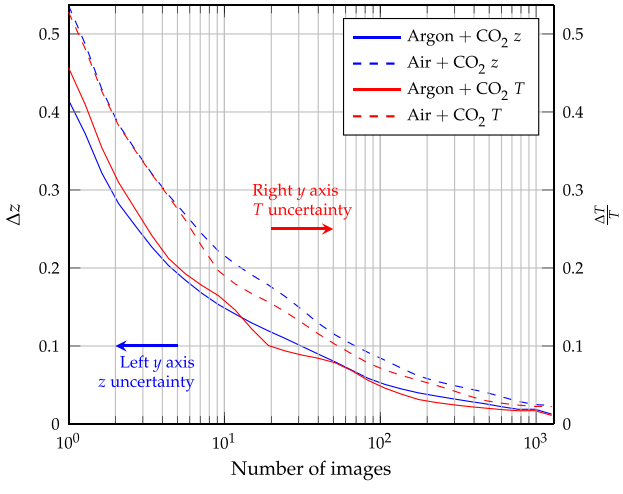

Fig. 12. Variation of maximum relative error for mixture fraction and temperature with number of images. Blue lines represent mixture fraction, red lines represent temperature, solid lines represent an argon/CO_2 mixture, and dashed lines represent an air/CO_2 mixture.

The maximum uncertainty criterion (Fig. 12) shows large values with almost 50% uncertainty present for both mixture fraction and temperature when taking only one image, using

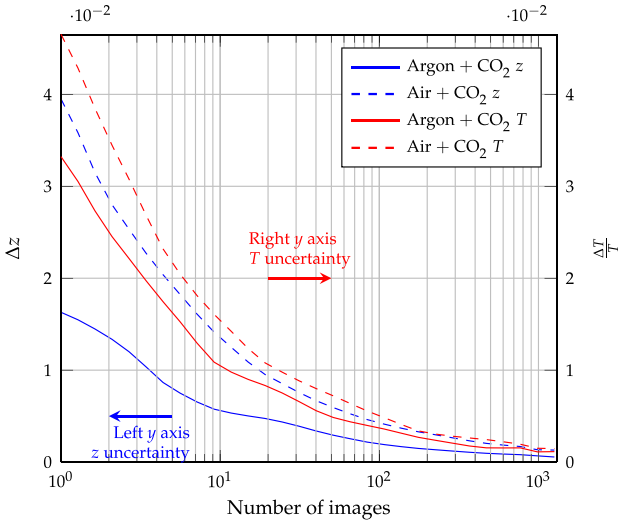

Fig. 13. Variation of mean relative error for mixture fraction and temperature with number of images. Blue lines represent mixture fraction, red lines represent temperature, solid lines represent an argon/CO_2 mixture, and dashed lines represent an air/CO_2 mixture.

both gas combinations. These large uncertainties were found to be isolated to a very small number of pixels and as such do not adequately represent the entire interrogation region. However, the trends shown in Fig. 12 match trends obtained using the average uncertainty criterion, confirming the effect of averaging multiple images. The average uncertainty criterion (Fig. 13), which is more representative of typical uncertainty across a whole image, shows significantly lower values. Nonetheless, it is worth noting that a 4% uncertainty in mixture fraction from a single image is present when using air and CO_2—this is of a similar magnitude to that of argon and CO_2, albeit higher (as expected). The temperature uncertainties scale similarly as a result of the temperature being calculated from the recovered mixture fraction. In both figures, it is evident that taking more images and averaging improves uncertainty. Averaging 10 pictures more than halves the uncertainty in all measurements, but only steady flow phenomena may be investigated this way. High-speed and turbulent flow measurements will inevitably rely on single-shot results in order to accurately resolve unsteady flow phenomena.

5. CONCLUSION

The aim of this work was to demonstrate the use of PDRS as a simultaneous mixture fraction and temperature diagnostic for non-isothermal gaseous mixtures. Such a validation would expand the application of this powerful diagnostic to a range of fluid dynamic research areas outside combustion and flames, where it has predominantly found use. A proof-of-concept experiment was performed where PDRS was successfully applied to a binary jet flow configuration. A mean SNR of 7.5 was achievable, leading to good quality results in a benchtop configuration. A numerical sensitivity analysis was also conducted to estimate the expected uncertainty from performing PDRS using different gas combinations. A framework for performing this analysis was elaborated, with results from two key gas combinations presented. It was demonstrated that gas combinations with large disparity in r_p produce smaller uncertainties, as indicated by a ∼2% mean uncertainty in z for an argon and CO_2 gas combination. Nonetheless, error of a similar order of magnitude in both mixture fraction and temperature can be expected for gas combinations with moderate disparity in r_p (air and CO_2), which shows that the technique could see more widespread adoption, particularly in wind-tunnel applications where the use of such gases is both more relevant and convenient.

Funding. Engineering and Physical Sciences Research Council (EP/P000878/1); Somerville College, University of Oxford.

Disclosures. The authors declare no conflicts of interest.

Data availability. Data underlying the results presented in this paper are available in Ref. [38].

REFERENCES

1. T. Hermann, M. McGilvray, and I. Naved, "Performance of transpiration-cooled heat shields for reentry vehicles," AIAA J. **58**, 830–841 (2020).
2. H. Boehrk, O. Piol, and M. Kuhn, "Heat balance of a transpiration-cooled heat shield," J. Thermophys. Heat Transfer **24**, 581–588 (2010).
3. Y. Jiang, A. Murray, P. Ireland, and L. Di Mare, "Coolant jets interaction in effusion cooling system: experimental and numerical study," in *Turbo Expo: Power for Land, Sea, and Air* (American Society of Mechanical Engineers, 2019), vol. **58646**, paper V05AT12A003.
4. J. Basley, K. Gouder, Y. Murai, C. Fradin, D. Glymond, L. Vandeperre, and J. Morrison, "Large-scale experimental study of the turbulent flow over an effusion cooling plate," Abstract, Bull. Am Phys. Soc. **63** (2018).
5. J. Yoo, V. Prikhodko, J. E. Parks, A. Perfetto, S. Geckler, and W. P. Partridge, "Fast spatially resolved exhaust gas recirculation (EGR) distribution measurements in an internal combustion engine using absorption spectroscopy," Appl. Spectrosc. **69**, 1047–1058 (2015).
6. W. M. Kays, "Turbulent Prandtl number. Where are we?" ASME J. Heat Transfer **116**, 284–295 (1994).
7. A. Vergara, E. Llobet, J. Brezmes, P. Ivanov, C. Cané, I. Grícia, X. Vilanova, and X. Correig, "Quantitative gas mixture analysis using temperature-modulated micro-hotplate gas sensors: selection and validation of the optimal modulating frequencies," Sens. Actuators B **123**, 1002–1016 (2007).
8. H. Eicker, "Method and apparatus for determining the concentration of one gaseous component in a mixture of gases," U.S. patent4,012,692 (15 March1977).
9. V. H. D. Le, "Method and apparatus for operating a gas sensor," U.S. patent3,906,473 (16 September1975).
10. S. Krishnan, B. M. Kumfer, W. Wu, J. Li, A. Nehorai, and R. L. Axelbaum, "An approach to thermocouple measurements that reduces uncertainties in high-temperature environments," Energy Fuels **29**, 3446–3455 (2015).
11. K. Farahmand and J. W. Kaufman, "Experimental measurement of fine thermocouple response time in air," Exp. Heat Transfer **14**, 107–118 (2001).
12. J. Gregory, K. Asai, M. Kameda, T. Liu, and J. Sullivan, "A review of pressure-sensitive paint for high-speed and unsteady aerodynamics," Proc. Inst. Mech. Eng. Part G **222**, 249–290 (2008).
13. A. C. Eckbreth, *Laser Diagnostics for Combustion Temperature and Species* (CRC press, 1996), Vol. **3**.
14. R. K. Hanson, "Combustion diagnostics: planar imaging techniques," Symp. (Int.) Combust. **21**, 1677–1691 (1988).
15. R. B. Miles, W. R. Lempert, and J. N. Forkey, "Laser Rayleigh scattering," Meas. Sci. Technol. **12**, R33–R51 (2001).
16. J. Panda and R. G. Seasholtz, "Measurement of shock structure and shock–vortex interaction in underexpanded jets using Rayleigh scattering," Phys. Fluids **11**, 3761–3777 (1999).

17. W. M. Pitts and T. Kashiwagi, "The application of laser-induced Rayleigh light scattering to the study of turbulent mixing," J. Fluid Mech. **141**, 391–429 (1984).
18. S. C. Graham, A. J. Grant, and J. M. Jones, "Transient molecular concentration measurements in turbulent flows using Rayleigh light scattering," AIAA J. **12**, 1140–1142 (1974).
19. K. Fiedler, O. Sieber, and C. Jakiel, "Quantitative density measurements by Rayleigh scattering behind a plane turbine cascade," AIAA J. **35**, 1303–1308 (1997).
20. S. H. Stårner, R. W. Bilger, R. W. Dibble, and R. S. Barlow, "Piloted diffusion flames of diluted methane near extinction: detailed structure from laser measurements," Combust. Sci. Technol. **72**, 255–269 (1990).
21. S. H. Stårner, R. W. Bilger, K. M. Lyons, J. H. Frank, and M. B. Long, "Conserved scalar measurements in turbulent diffusion flames by a Raman and Rayleigh ribbon imaging method," Combust. Flame **99**, 347–354 (1994).
22. S. H. Stårner, R. W. Bilger, J. H. Frank, D. F. Marran, and M. B. Long, "Mixture fraction imaging in a lifted methane jet flame," Combust. Flame **107**, 307–313 (1996).
23. S. H. Stårner, R. W. Bilger, M. B. Long, J. H. Frank, and D. F. Marran, "Scalar dissipation measurements in turbulent jet diffusion flames of air diluted methane and hydrogen," Combust. Sci. Technol. **129**, 141–163 (1997).
24. A. Sevault, M. Dunn, R. S. Barlow, and M. Ditaranto, "On the structure of the near field of oxy-fuel jet flames using Raman/Rayleigh laser diagnostics," Combust. Flame **159**, 3342–3352 (2012).
25. J. H. Frank, K. M. Lyons, D. F. Marran, M. B. Long, S. H. Stårner, and R. W. Bilger, "Mixture fraction imaging in turbulent nonpremixed hydrocarbon flames," in *Symposium (International) on Combustion* (Elsevier, 1994), Vol. **25**, pp. 1159–1166.
26. J. Fielding, J. H. Frank, S. A. Kaiser, M. D. Smooke, and M. B. Long, "Polarized/depolarized Rayleigh scattering for determining fuel concentrations in flames," Proc. Combust. Inst. **29**, 2703–2709 (2002).
27. J. H. Frank, S. A. Kaiser, and M. B. Long, "Reaction-rate, mixture-fraction, and temperature imaging in turbulent methane/air jet flames," Proc. Combust. Inst. **29**, 2687–2694 (2002).
28. J. H. Frank, S. A. Kaiser, and M. B. Long, "Multiscalar imaging in partially premixed jet flames with argon dilution," Combust. Flame **143**, 507–523 (2005).
29. M. F. Zulkifli, F. Beyrau, and B. Williams, "Temperature, OH and CH2O structure in the near field of oxy-fuel flames," in *8th European Combustion Meeting* (2017).
30. J. R. Smith, "Rayleigh temperature profiles in a hydrogen diffusion flame," Proc. SPIE **158**, 84–91 (1978).
31. V. Bergmann, W. Meier, D. Wolff, and W. Stricker, "Application of spontaneous Raman and Rayleigh scattering and 2D LIF for the characterization of a turbulent $CH_4/H_2/N_2$ jet diffusion flame," Appl. Phys. B **66**, 489–502 (1998).
32. R. W. Dibble and R. E. Hollenbach, "Laser rayleigh thermometry in turbulent flames," in *Symposium (International) on Combustion* (Elsevier, 1981), Vol. **18**, pp. 1489–1499.
33. F. Fuest, R. S. Barlow, J. Y. Chen, and A. Dreizler, "Raman/Rayleigh scattering and CO-LIF measurements in laminar and turbulent jet flames of dimethyl ether," Combust. Flame **159**, 2533–2562 (2012).
34. J. A. Sutton and J. F. Driscoll, "Rayleigh scattering cross sections of combustion species at 266, 355, and 532 nm for thermometry applications," Opt. Lett. **29**, 2620–2622 (2004).
35. W. C. Gardiner, Jr., Y. Hidaka, and T. Tanzawa, "Refractivity of combustion gases," Combust. Flame **40**, 213–219 (1981).
36. J. Bouguet and P. Perona, "Camera calibration from points and lines in dual-space geometry," in *5th European Conference on Computer Vision* (Citeseer, 1998), pp. 2–6.
37. W. Schottky, "On spontaneous current fluctuations in various electrical conductors," J. Micro/Nanolithogr. MEMS MOEMS **17**, 041001 (2018).
38. K. Chakravarthy, L. M. Le Page, and B. A. O. Williams, "Data for 'Polarised-depolarised Rayleigh scattering for simultaneous composition and temperature measurements in non-isothermal gaseous mixtures'," University of Oxford, 2023, https://ora.ox.ac.uk/objects/uuid:8067185e-0634-4637-910b-9122404b70cd.